

(This is a sample cover image for this issue. The actual cover is not yet available at this time.)

This article appeared in a journal published by Elsevier. The attached copy is furnished to the author for internal non-commercial research and education use, including for instruction at the authors institution and sharing with colleagues.

Other uses, including reproduction and distribution, or selling or licensing copies, or posting to personal, institutional or third party websites are prohibited.

In most cases authors are permitted to post their version of the article (e.g. in Word or Tex form) to their personal website or institutional repository. Authors requiring further information regarding Elsevier's archiving and manuscript policies are encouraged to visit:

<http://www.elsevier.com/copyright>



Contents lists available at SciVerse ScienceDirect

Applied Clay Science

journal homepage: www.elsevier.com/locate/clay

Mineral assemblages and distribution of phyllosilicates composition along the main section of the Agua Rica deposit, Catamarca, Argentina. Implications for future mine development

Marta Franchini ^{a,b,*}, Agnes Impiccini ^b, Daniel Beaufort ^c, Patricia Patrier ^c,
Corby G. Anderson ^d, Josefina Pons ^{a,b}

^a Consejo Nacional de Investigaciones Científicas y Técnicas, Centro Patagónico de Estudios Metalogenéticos, Argentina

^b Departamento de Geología y Petróleo, Facultad de Ingeniería, Universidad Nacional del Comahue, Buenos Aires 1400, (8300) Neuquén, Argentina

^c Université de Poitiers, IC2MP, CNRS-UMR 7285, Hydras, Bâtiment B08, Rue Albert Turpin, F-86022 Poitiers Cedex, France

^d Kroll Institute for Extractive Metallurgy George S. Ansell Department of Metallurgical and Materials Engineering, Colorado School of Mines, Golden, CO, USA

ARTICLE INFO

Article history:

Received 12 April 2011

Received in revised form 7 May 2012

Accepted 27 May 2012

Available online xxxx

Keywords:

Porphyry Cu–Mo

High sulfidation epithermal

Phyllosilicate minerals

Flotation, metal recovery

ABSTRACT

Agua Rica (27°26'S–66°16'O) is a world class Cu (Mo–Au) deposit located in Catamarca, Argentina, in which the porphyry and high sulfidation epithermal stages usually distant 1 km vertically, are located at the same level of erosion. Seventy one samples and 120 phyllosilicates were analyzed from the study section (E–W 6969400 N) to determine distinctive mineralogical zones which differ not only by their hydrothermal history but also by their potential behavior during the ore processing operations via flotation. In the east side of the section, biotite $K_{1.78-1.67} Na_{0.05-0.02}(Al_{0.42-0.00}Mg_{3.77-3.22}Fe_{1.46-1.00}Ti_{0.90-0.18}Mn_{0.02-0.01})(Si_{5.42-4.82}Al_{3.18-2.58})(OH_{1.90-1.40}Cl_{0.06-0.04})_4$ of the early, high temperature potassic alteration (>550 °C to 370 °C) is encapsulated in a phyllic halo dominated by illite $K_{1.73-1.08} Na_{0.10-0.0}(Al_{3.96-3.49}Mg_{0.36-0.03}Fe_{0.25-0.01}Ti_{0.06-0.0})(Si_{6.53-6.07}Al_{1.93-1.47})(OH_{0.54-0.0}Cl_{0.02-0.0})_4$ + quartz + pyrite + covellite + molybdenite + rutile. This mineral assemblage formed from fluids with temperatures ≤350 °C that attained high sulfur fugacity. The clasts of the hydrothermal and mineralized breccia bodies located at the center of the section and to the east contain widespread pyrophyllite $K_{0.05-0.0}(Al_{4.07-3.94}Fe_{0.12-0.01})(Si_{7.92-7.50}Al_{0.50-0.05})(OH_{0.15-0.02}Cl_{0.03-0.0})_4$ that had replaced illite at temperatures between 360 °C and 280 °C. Minor amounts of dickite and widespread kaolinite occur in the advanced argillic and phyllic halos, respectively, as late minerals in clots or in veinlets thus, fluids cooled enough (<270° and <200 °C, respectively) for their formation. The presence of phyllosilicate minerals is a potential cause of loss in recovery of copper and molybdenite during the flotation process. Carefully planned and controlled comprehensive liberation and flotation testing should be undertaken in conjunction with mineralogical analysis to optimize and quantify recoveries, separations, grades and gangue deportment.

© 2012 Elsevier B.V. All rights reserved.

1. Introduction

Agua Rica is a world class Cu (Mo–Au) polymetallic deposit located in Catamarca, Argentina (27° 26' S–66° 16' O). It has an estimated resource total 797 Mt of 0.49% Cu, 0.23 g/t Au, 0.03% Mo, and 3.62 g/t Ag (Yamana Gold 2006, Feasibility Study Update; www.yamana.com). With the Bajo de la Alumbrera porphyry Cu–Au located 40 km west, they constitute the major Cu–Mo–Au resources of the Miocene Farallón Negro Volcanic Complex.

In Agua Rica, both the mesothermal porphyry and high sulfidation epithermal stages which are 1 km vertically distant in most of the porphyry systems worldwide are located at the same level of erosion.

Koukharsky and Mirré (1976), Navarro (1986), Sasso (1997), Perelló et al. (1998), BHP (1999), and Landtwing et al. (2002) document a complex history of overprinting stages of subvolcanic intrusions, mineralization, brecciation, and erosion at Agua Rica. Recent study of the hydrothermal alteration and mineralization stages along the east–west 6969400 N main section provide additional insights into the time–space framework for the episodic superposition of multiple igneous and related hydrothermal breccia events, which coalesced into a Cu–Mo–Au–Zn–Pb ore shell (Franchini et al., 2011). This investigation also showed that the various types of alteration zones formed around mineralization are dominated by phyllosilicates, indicating the importance of alteration zones in the formation of industrial clay deposits.

In this study we present a detailed mineralogical study of phyllosilicates and their distribution along an east–west cross-section through the main part of the deposit. The objective of this contribution was to provide key information on these hydrothermal minerals which

* Corresponding author at: Departamento de Geología y Petróleo, Facultad de Ingeniería, Universidad Nacional del Comahue, Buenos Aires 1400, (8300) Neuquén, Argentina. Tel.: +54 299 4485344x4488307; fax: +54 299 4485344.

E-mail address: mfranchini@speedy.com.ar (M. Franchini).

are necessary (1) to add elements for a well constrained time-space framework for the porphyry-epithermal transition in which phyllosilicate minerals may be used to document the thermal and chemical evolution of a complex system like Agua Rica; and (2) to optimize the orebody metallurgy management during the upcoming economic mine development.

2. Geology of the deposit

The Agua Rica deposit is localized in the Sierra del Aconquija, one of the uplift blocks of the Sierras Pampeanas basement, 200 km east of the Cordillera de los Andes (Fig. 1). The oldest rocks in the region are Precambrian to Early Paleozoic schistose and massive metasedimentary rocks (Fig. 1) (Koukharsky and Mirré, 1976). These metamorphic rocks were folded and intruded by Paleozoic granitic plutons and pegmatites (422.7 ± 6.1 and 438.4 ± 6.3 Ma, K–Ar muscovite ages; Capillitas–Belén granite suite; (Caelles et al., 1971; Koukharsky and Mirré, 1976) (Fig. 1). During the Miocene, a series of porphyritic stocks intruded the country rocks (Fig. 1) (Navarro, 1986; Perelló et al., 1998; Sasso, 1997; Sasso and Clark, 1998). Landtwing et al. (2002) identified and described in detail various breccia types in the Agua Rica district. According to these authors the hydrothermal breccia exposed along the Quebrada Minas lineament is volumetrically the most prominent (Fig. 1) and shows textural and compositional variations. Several small porphyritic bodies have been mapped at the margin of the deposit (distal porphyries; Landtwing et al., 2002) (Fig. 1). The porphyries and breccias were

emplaced along the SE-striking Quebrada Minas lineament (Fig. 1). East–west striking, south-dipping normal faults were active both syn- and post-mineralization. The Quebrada Seca fault (Fig. 1) offsets leached material, and epithermal fluids moved along the same structure (see Landtwing et al., 2002).

2.1. Summary of geology, alteration and mineralization

The east–west main section (6969400 N) of the Agua Rica deposit was selected for this study (Fig. 1). Fig. 2A to C show the geology, alterations and Cu–Mo–Au geochemistry. The geology of this section consists of the Seca Norte and the Trampeadero porphyries that intruded the metasedimentary rocks and are cut by igneous and hydrothermal breccias. Relics of early potassic alteration features with Cu (Mo–Au) mineralization were encapsulated in the subsequent phyllic halo with pyrite + covellite ore assemblage and molybdenite in stringers and B-type (Gustafson and Hunt, 1975) quartz veinlets. The advanced argillic alteration intensely overprinted the potassic-phyllic alteration zones and their related quartz veinlets, and Cu–Mo–Au mineralization in both porphyries and the metasedimentary rocks. Such a later alteration has been associated with the generation of a continuous suite of interfingering igneous and hydrothermal breccias (Landtwing et al., 2002). This alteration type is centered in the Seca Norte hydrothermal breccias (drill hole AR-82) with textures of intense acid leaching (residual quartz). The hydrothermal breccias continues east, affecting the upper levels of the Trampeadero porphyry (drill hole AR-18) and

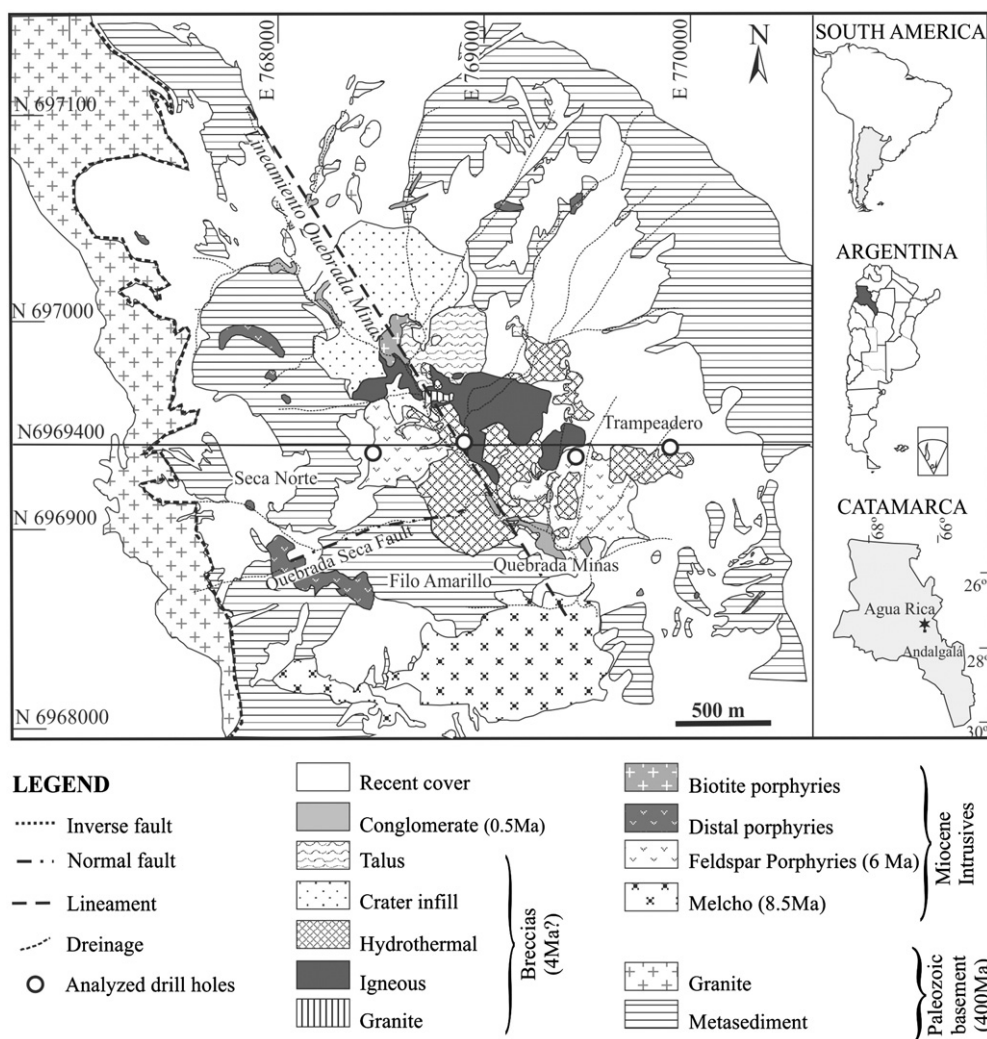


Fig. 1. Geological map of the Agua Rica district with the location of the E-06969400 N cross section and sampled drill holes (modified from BHP, 1999 and Landtwing et al., 2002).

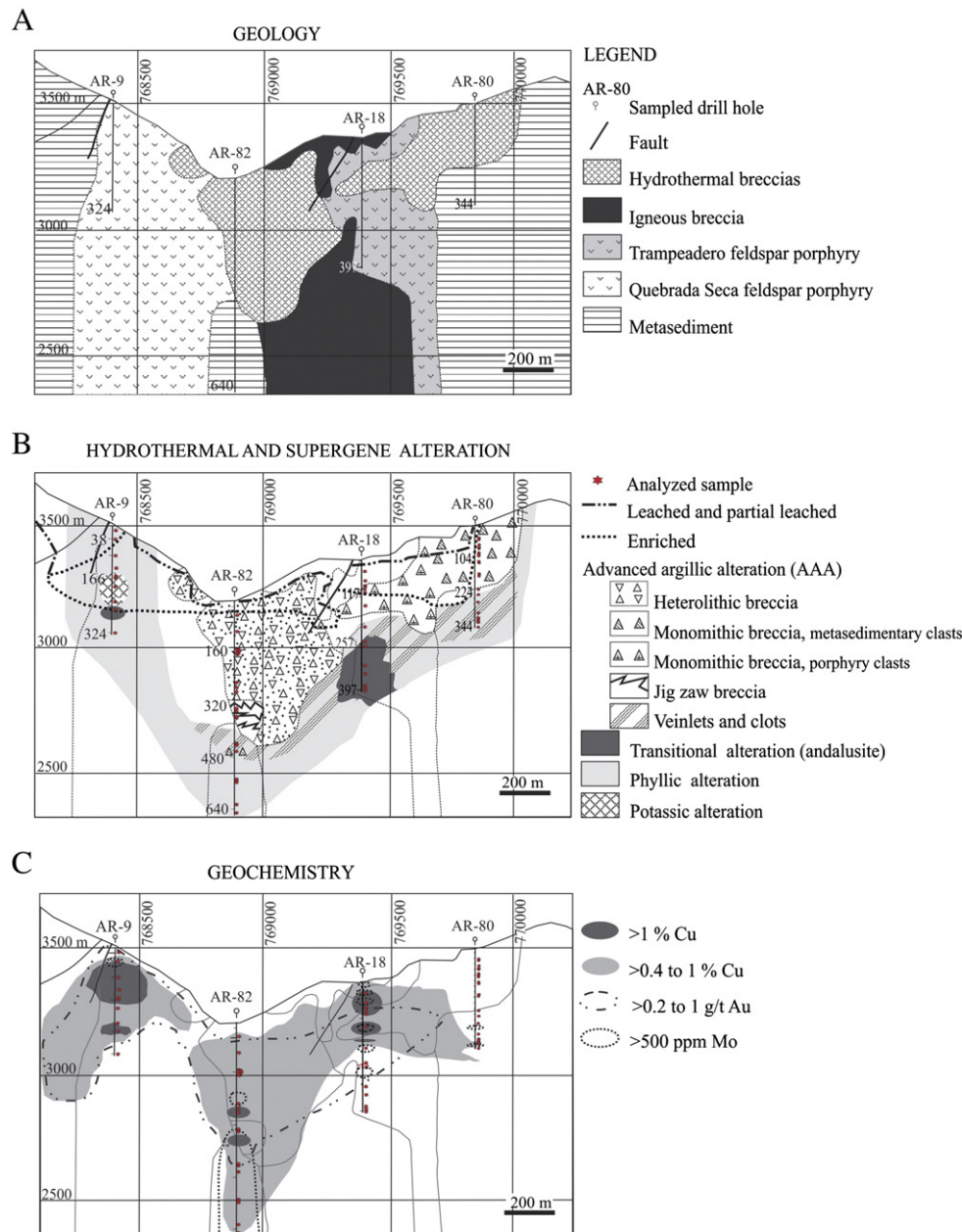


Fig. 2. A) Geology of the E–O section along 6969400 N with the location of sampled drill holes and analyzed samples. B) Lateral and vertical distribution of hydrothermal and supergene alteration types along the section. C) Geochemistry of the section (modified from BHP, 1999 and Franchini et al., 2011).

the metasedimentary rocks (drill hole AR-80). It has been divided in a barren, pre-brecciation stage and several post-brecciation Cu–As–, Au–Bi, and Zn–Pb mineralization stages (Franchini et al., 2011).

3. Materials and methods

3.1. Materials

The samples investigated in this work consist of seventy one samples of hydrothermally altered rocks that were collected from 4 drill cores owned by BHP (10 samples of AR-9, 24 of AR-82, 16 of AR-18, and 21 of AR-80). Figs. 1 and 2A to C show drill hole locations in the east–west section 6969400 N across the Agua Rica deposit. Textures and alteration petrography were analyzed in thin sections of drill cores with a binocular optical polarizing microscope.

3.2. X-ray diffraction

The minerals were identified using a Rigaku DMAX-2D diffractometer at the Centro de Investigaciones en Minerales Arcillosos de la Universidad Nacional del Comahue, Neuquén. Bulk samples ($n = 71$) and the clay fraction ($<2 \mu\text{m}$) were analyzed from 2° to $40^\circ 2\theta$, at 2° /min, with $\text{CuK } \alpha^{1+2}$ radiation, run at 40 kV and 20 mA. The XRD reflections were evaluated with Rigaku software. For all samples, clay minerals were identified by X-Ray diffraction (XRD) on oriented mounts of the less than $2 \mu\text{m}$ fraction size as oriented aggregates. Whole-rock samples (each corresponding to half pieces of drill core approximately 8 cm long and 2 cm thick) were crushed and ground with a mortar and pestle and then 30 g of each powdered whole rock were added to one liter of distilled water and dispersed by ultrasonic probe. The $<2 \mu\text{m}$ fraction was separated by timed centrifugation. Oriented preparations of Sr-saturated $<2 \mu\text{m}$ fraction were

analyzed by means of X-Ray diffraction (XRD) in air-dried (AD) state (drying at room conditions), ethylene glycol (EG) solvation, and heating to 375 °C and 550 °C for one hour. The quantitative clay analyses were carried out using the Mineral Intensity Factor (MIF) method described in Moore and Reynolds (1997).

Layer-charge characteristics of smectite from 4 samples containing this mineral were determined following the method of Christidis and Eberl (2003). The samples were dispersed in distilled water using an ultrasonic probe. The <1 µm fraction was separated by settling and then saturated twice with K using 1 N KCl. The K-smectites were centrifuged, dialyzed until chloride free, dried on Si wafers at room temperature, and then were solvated with ethylene glycol vapor at 60 °C. Oriented samples were analyzed by means of X-Ray diffraction (XRD).

For the determination of polytypes, the <1 µm size fraction of randomly oriented powders was analyzed using a Rigaku DMAX-2D X-ray diffractometer (XRD). The samples were top-packed due to the small amount of sample. The powders were run in step scanning mode (0.02 degrees per step) from 16 to 44 degrees 2θ and a 20 seconds count time. Relative abundance of illite, I-S, pyrophyllite and kaolinite and/or dickite in the clay-size fraction was estimated from integrated peak intensities on diffraction patterns of oriented clays on the glass slide X-ray mounts. The method used, described by Moore and Reynolds (1997), gives the relative proportions of the clay minerals normalized to 100 percent. Mineral intensity factors required in the method are calibration constants for the intensities of diffraction peaks that allow quantitative estimation of relative proportions of each mineral in the mixture. The mineral intensity factors calculated for these diffraction peaks were completed using program NEWMOD© (Reynolds and Reynolds, 1996). The intensity ratio (Ir) for illite was calculated from the intensity (I) of d(001) and d(003) X-ray diffraction peaks in air dried (A.D.) and ethylene glycol solvated (E.G.) samples (i.e., $Ir = I(001) / I(003)$ A.D./I(001)/I(003) E.G.). The Ir value will be <1 if no expanding component is present and >1 if a swelling component (smectite) is interstratified. As 005 reflection of discrete smectite and 101 reflection of quartz partially overlap the 003 reflection of illite Ir was measured on samples where mineral overlapping were minimum.

Kaolinite and dickite identification were based on data of infrared spectroscopy. Infrared (IR) spectra were recorded in the 3800–200 cm⁻¹ range on a Nicolet 510 FT-IR spectrometer with a 4 cm⁻¹ resolution using KBr pressed pellets heated to 110 °C overnight. The disks of 2 cm diameter were prepared by mixing a 2 mg sample with 300 mg KBr. In the hydroxyl-stretching band region of phyllosilicates (i.e., 3500–3800 cm⁻¹), the diagnostic bands are 3695, 3668, 3652 and 3621 cm⁻¹, respectively for kaolinite and 3710, 3655 and 3620 cm⁻¹ for dickite (Brindley et al., 1986).

3.3. Microprobe analysis of phyllosilicates

Phyllosilicates compositions were determined by electron microprobe analyses (EPMA) ($n=120$) at the Microanalytical facility at the University of New Brunswick (Canada); mineral compositions were determined in wavelength-dispersion mode on a JXA JEOL-733 Superprobe, with 15 kV accelerating voltage, 10 nA beam current, and a maximum 40 s counting interval. The beam size on the sample was 5 µm. A combination of various mineral and metal standards were used and ZAF matrix corrections have been done by means of CITZAF version 3.03 (J.T. Armstrong, 1997, shareware; Division of Earth and Planetary Sciences, the California Institute of Technology).

4. Results

4.1. Biotite

Secondary biotite from potassic alteration facies identified in the Seca Norte porphyry at 166, 187.7, and 223 m depth (Fig. 3), occurs as aggregates of very fine brownish plates (from 0.05 to 0.3 mm)

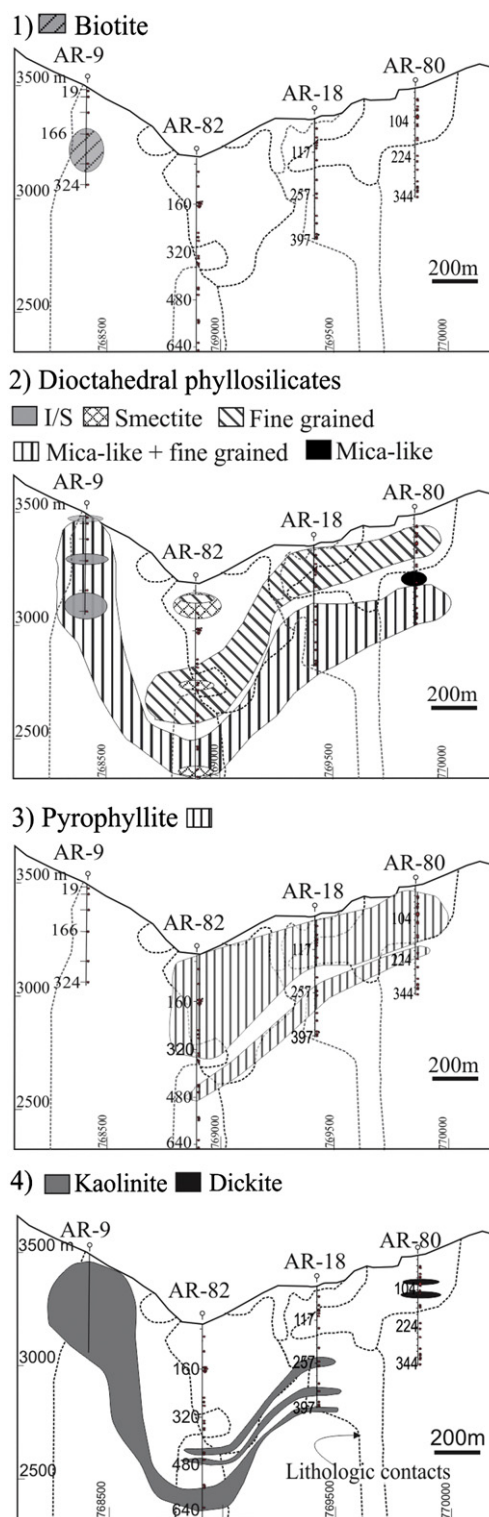


Fig. 3. Distribution of biotite and phyllosilicates of the potassic and phyllic alterations and pyrophyllite, dickite, and kaolinite of the advanced argillic alteration along the E-O6969400 N cross section.

replacing previous igneous ferromagnesian silicates (biotite and amphibole). They commonly consist in irregular biotite stringers. Both chemical composition and structural formulas of secondary biotites are presented in Table 1.

The structural formula of biotite from analyses (Table 1) was recalculated for 22 oxygen atoms (Moore and Reynolds, 1997).

Table 1
Representative microprobe analyses of hydrothermal biotite.

Sample	AR09–166 m							
(wt.%)								
SiO ₂	38.63	36.97	37.44	36.21	36.14	36.14	38.88	36.61
TiO ₂	2.17	2.18	1.69	1.70	2.60	1.40	2.29	2.60
Al ₂ O ₃	16.04	17.41	17.40	19.06	18.64	18.83	15.33	16.79
¹ FeO	11.14	11.96	12.02	12.20	11.68	8.98	10.48	11.52
MnO	0.07	0.08	0.08	0.16	0.18	0.10	0.13	0.12
MgO	17.98	16.93	17.48	15.05	16.05	17.61	18.15	16.65
CaO	0.00	0.00	0.01	0.00	0.00	0.00	0.00	0.00
SrO	0.05	0.05	0.05	0.04	0.08	0.04	0.05	0.05
BaO	0.14	0.08	0.00	0.00	0.00	0.05	0.10	0.05
Na ₂ O	0.12	0.13	0.11	0.09	0.09	0.11	0.18	0.12
K ₂ O	9.81	9.85	9.56	9.64	9.75	9.83	9.66	9.69
F	4.15	3.61	3.56	3.40	3.11	3.52	4.38	3.78
Cl	0.24	0.23	0.21	0.19	0.25	0.16	0.24	0.23
P ₂ O ₅	0.02	0.00	0.00	0.00	0.01	0.02	0.00	0.01
Total	98.75	97.90	98.05	96.27	97.23	95.28	97.97	96.57

Structural formulae based on 22 oxygen atoms								
Tetrahedral								
^{IV} Si	5.37	5.23	5.27	5.20	5.15	4.82	5.42	5.24
^{IV} Al	2.63	2.78	2.73	2.80	2.85	3.18	2.58	2.76
Octahedral								
^{VI} Al	0.00	0.13	0.15	0.42	0.28	0.00	0.00	0.00
Ti	0.23	0.23	0.18	0.18	0.28	0.90	0.24	0.28
Fe	1.30	1.41	1.41	1.46	1.39	1.00	1.22	1.38
Mn	0.01	0.01	0.01	0.02	0.02	0.01	0.02	0.01
Mg	3.73	3.57	3.67	3.22	3.41	3.50	3.77	3.55
ΣVI	5.25	5.35	5.42	5.31	5.38	5.41	5.25	5.22
Ca	0.00	0.00	0.00	0.00	0.00	0.00	0.00	0.00
Na	0.03	0.04	0.03	0.03	0.02	0.03	0.05	0.03
K	1.74	1.78	1.72	1.77	1.77	1.67	1.72	1.77
Ba	0.01	0.00	0.00	0.00	0.00	0.00	0.01	0.00
Sr	0.00	0.00	0.00	0.00	0.00	0.00	0.00	0.00
Σ Interlayer	1.78	1.82	1.75	1.79	1.80	1.70	1.77	1.80
F	1.82	1.61	1.58	1.54	1.40	1.48	1.90	1.71
Cl	0.06	0.06	0.05	0.05	0.06	0.04	0.06	0.06
XMg	0.74	0.72	0.72	0.69	0.71	0.78	0.76	0.72

1. All iron as Fe²⁺.

ΣVI: sum of octahedral cations.

Representative biotite crystals have the compositional range K_{1.78–1.67}Na_{0.05–0.02}(Al_{0.42–0.00}Mg_{3.77–3.22}Fe_{1.46–1.00}Ti_{0.90–0.18}Mn_{0.02–0.01})(Si_{5.42–4.82}Al_{3.18–2.58})(OH_F_{1.90–1.40}Cl_{0.06–0.04})₄. K is by far the dominant cation in the interlayer with only traces of Na. Mg largely predominates over Fe (arbitrarily considered as Fe²⁺) in the octahedral site which is completed by small amounts of Ti, Al, and Mn²⁺. Biotite grains have Mg/(Mg + Fe) (*X*_{Mg}) values between 0.69 and 0.78 and locally very high F content (>3.4% F). Such a high *X*_{Mg} incorporates more F, a crystal-chemical effect referred to as the Fe-F avoidance principle (Munoz, 1984). Plotted in the diagram of Fe²⁺/(Fe²⁺ + Mg) versus Al^{IV} content, the structural formulas of the secondary biotites fall in the phlogopite field (Fig. 4). Plotted in the MR³–2R³–3R² coordinates

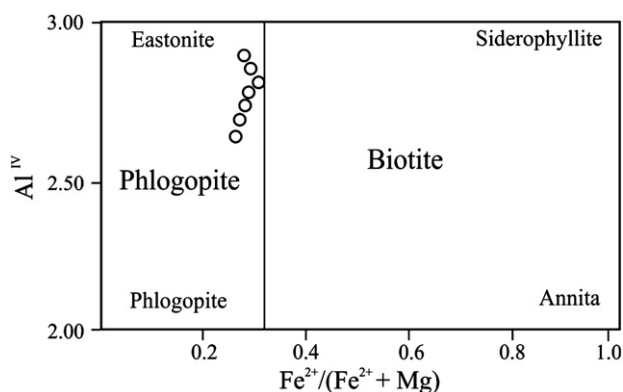


Fig. 4. Biotite composition from the potassic zone (modified from Deer et al., 1992).

(Fig. 5) the structural analyses of such biotite are similar to those of relic biotites in the phyllic halo of other porphyry Cu deposits (see Beaufort and Meunier, 1983; Selby and Nesbitt, 2000).

4.2. Potassic dioctahedral phyllosilicates

Mica-like (>2 μm) + fine grained (<2 μm) dioctahedral potassic phyllosilicates occur in most of the phyllic envelope, mica-like only in a sector of the metasediment with phyllic alteration cut by drill hole AR-80, and fine grained phyllosilicate alone occurs in the advanced argillic alteration zone, in breccias clasts and clay matrix in association with pyrophyllite (Fig. 3). They are accompanied by quartz + pyrite + covellite + molybdenite + rutile as patches or clots replacing the porphyries, and fine-grained disseminations or segregations replacing the metasediment. Illite was identified by XRD in the <2 μm fraction of the 53 analyzed samples. Illite was distinguished in air-dried, ethylene glycol-saturated, and calcinated samples by the sharp reflection of the 001 peak at 10 Å, and by rational 2nd, 3rd, and 4th order reflections. Based on the illite intensity ratio (Ir), with values between 0.92 and 0.99, no expandable layers were found, except for illite from samples AR-9 166 m and 264 m, with an Ir between 1.03 and 1.29 that corresponds to an interstratified I-S type R0, with a high proportion of smectite layers (~90% according to Moore and Reynolds, 1997) (Fig. 6A). The illite polytype determined in the <1 μm fraction of 12 samples corresponds to 2M₁.

The analytical results from 45 microprobe analyses for white micas (summarized in Table 2) are: K_{1.73–1.08}Na_{0.10–0.0}(Al_{3.96–3.49}Mg_{0.36–0.03}Fe_{0.25–0.01}Ti_{0.06–0.0})(Si_{6.53–6.07}Al_{1.93–1.47})(OH_F_{0.54–0.0}Cl_{0.02–0.0})₄. Based on these results, all analyzed micas have less K and Na and more Si than theoretical dioctahedral micas (muscovite or phengite). The composition of most of them agree with that of illite (layer charge between 1.5 and 1.8) with a low extent of Tschermak substitution (Si + (Fe,Mg)²⁺ = Al^{IV} + Al^{VI}). However, most of the structural formulas display an unusually high octahedral occupancy (up to 4.2) which seems due to a slight excess of aluminum. In a few samples (AR 9 166 and 264 m) some structural formulas indicated interlayer charge which are much lower than those required for illite, suggesting the presence I-S mixed layers or smectite layers. However in this case, the analyses do not indicate any increase in exchangeable cations such as Ca, Mg or Na that are typical of expandable smectite layers. These two aforementioned characteristics argue in the sense of Al-rich mineral impurities in the volumes of potassic dioctahedral phyllosilicates analyzed investigated by the electron microprobe.

The chemical compositions of the potassic dioctahedral phyllosilicates analyzed in this study have been plotted in both the MR³–2R³–3R²

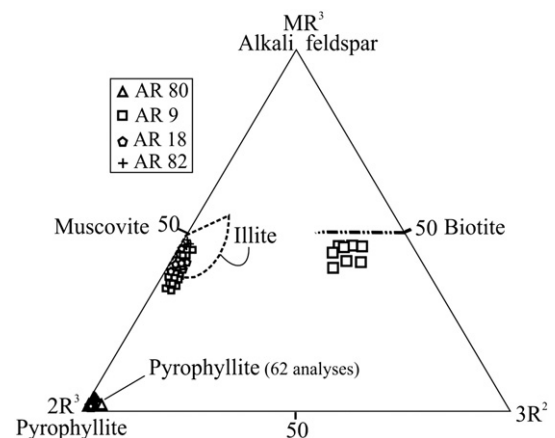


Fig. 5. Plot of the phyllosilicate compositions in the MR³–2R³–3R² triangle in which silica is considered as a component in excess, MR³ = Na + K + 2Ca; 2R³ = ((Al + Fe³⁺) – MR³)/2, and 3R² = (Mg + Mn + Fe²⁺)/3 (Velde, 1985). The range of compositions of the major phyllosilicates (biotite, alkali feldspar, muscovite, illite, pyrophyllite) based on Velde (1985).

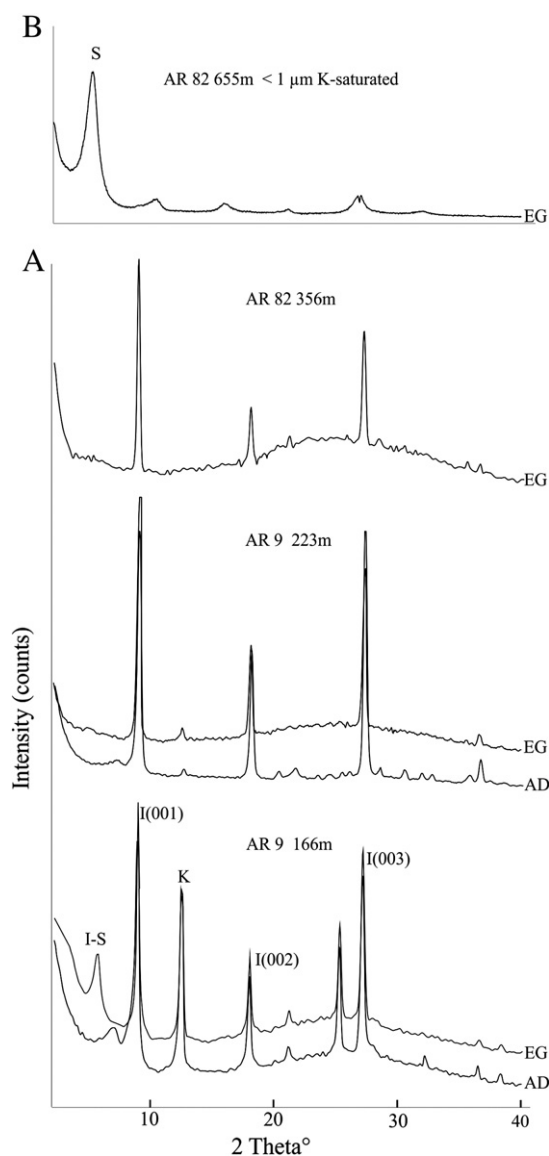


Fig. 6. A—Comparative analysis of the XRD patterns in samples with and without mixed layers clay mineral. AR-9 166 m: the asymmetry of the illite basal reflections I_{001} , I_{002} , I_{003} with a shift of I_{001} towards the low-angle side of the XRD pattern (towards I-S) after glycol solvation, indicates the presence of interstratified expandable layers (I+I-S < 10%) with ~90% smectite layers (R0) (Ir: 1.10). AR-9 223 m: The amount of I-S decreases (I+I-S traces). AR-82 356 m: the illite reflections are symmetrical and were not displaced to lower angles denoting the absence of mixed-layered structure (Ir < 1). B—Representative XRD patterns from oriented samples of K-saturated smectites (Christidis and Eberl, 2003). The first-order reflections are at 17 Å and the basal reflections are well defined.

(Fig. 5) and the muscovite–celadonite–pyrophyllite (Fig. 7) triangular coordinates (Newman and Brown, 1987; Velde, 1985). No analysis of true muscovite have been obtained in these diagrams and all analyses plot in the illite field except the data of samples AR-9 at 166 m and 264 m in which I-S mixed layer minerals have been identified by X-ray diffraction. In contrast to muscovite, the interlayer charge is significantly less than 2 (interlayer charge near 1.6), and Si in the tetrahedral site range between 6.1 and 6.5 in most of the analyses of illite.

4.3. Smectite (dioctahedral type)

Discrete smectite has been identified by X-ray diffraction in the central zone cut by drillhole AR 82, one sample comes from the deepest part of the phyllic envelope (AR-82 at 655.50 m) and the others come from hydrothermal breccias in both the intermediate

and upper part of the advanced argillic alteration zone (Fig. 3). The fact that the amount of smectite is less than 10 vol% in the samples and the absence of identified smectite matrix in thin section prevent the chemical analyses of this expandable phyllosilicate. Smectite was identified by its characteristic basal and 060 X-ray diffraction (Moore and Reynolds, 1997). Oriented homo-ionic Sr^{++} samples saturated with ethylene glycol (EG) display and increase $d_{001} = 12.3$ Å at 17 Å with solvation treatment and collapsed to 9.9 Å after heating at 550 °C. The $d_{006} = 1.502$ Å value derived from XRD pattern of randomly oriented powdered samples indicates its dioctahedral character.

Representative XRD patterns from oriented samples of K-saturated smectites are shown in Fig. 6B. These smectites have a small total layer charge because the first-order reflections are at 17 Å, their higher-order basal reflections are well defined, and do not contain fractions of 13.5 and 9.98 Å layers (Christidis and Eberl, 2003). Based on this data, the layer charged for the Agua Rica smectites is less than -0.4 (Christidis and Eberl, 2003).

4.4. Pyrophyllite

Pyrophyllite is widespread in the advanced argillic alteration zone (Fig. 3) and occurs with diasporite and zunyite up to 480 m depth in the centrally located heterolithic and monolithic jigsaw breccias. Pyrophyllite occurs with diasporite up to 270 m in the Trampeadero monolithic breccia and further east, with zunyite up to 160 m depth and with alunite up to 214 m in the brecciated metasediment. However, in all cases pyrophyllite predates the formation of diasporite, zunyite, and alunite. Pyrophyllite was distinguished by its X-ray reflections at 9.20, 4.42, and 3.07 Å, respectively, in air-dried samples, after ethylene glycol saturation, and in calcinated samples. Table 3 summarizes the chemical compositions ($n=62$) of pyrophyllite and the structural formula was recalculated on the basis of 22 oxygens. The analytical results from microprobe analyses of representative crystals are $\text{K}_{0.05-0.0}(\text{Al}_{4.07-3.94}\text{Fe}_{0.12-0.01})(\text{Si}_{7.92-7.50}\text{Al}_{0.50-0.05})(\text{OHF}_{0.15-0.02}\text{Cl}_{0.03-0.0})_4$. The Si/R³ ratios, ranging from 1.88 to 2, slightly deviate from the ideal ratio of 2. Thus, as already noted for illite, the Al content of the structural formulas of most of the pyrophyllite is slightly higher than that of a theoretical formula of pyrophyllite. The number of Al atoms is lower than 0.50 in the tetrahedral site, which represents only 6% of the tetrahedral cations, and makes up about 99% of the octahedral cations. Most analyses have total interlayer cations less than 0.05 and fluorine in a range from 0.15 to 0.02 replacing the OH site and this replacement is higher in pyrophyllite samples from the heterolithic and the Trampeadero monolithic breccias. Pyrophyllite compositions are represented in the system $\text{MR}^3\text{-}2\text{R}^3\text{-}3\text{R}^2$ (Velde, 1985) (Fig. 5). The compositional fields of typical hydrothermal pyrophyllite compiled by Newman and Brown (1987) are shown for comparison.

4.5. Dickite and kaolinite

The distinction between kaolinite and dickite were based on data of infrared spectroscopy. Dickite veinlets have been identified as overprinting early assemblages in the monolithic breccia intersected by drillhole AR-80 (Fig. 3). Kaolinite has been identified in the phyllic halo as a late mineral in clots that fill interstices between white micas of the phyllic halo (AR-9, AR-18) or in veinlets (AR-82 440 and 460 m) and in the monolithic breccias of the Trampeadero porphyry (AR-18 147 m) and the metasedimentary rocks (AR-80 83.6 and 113 m).

5. Discussion

5.1. Contribution of phyllosilicates to better constrain the time-space framework for the porphyry-epithermal transition

At Agua Rica, deep, intermediate and shallow hydrothermal mineral assemblages are now exposed at the same level of erosion. The

Table 2
Representative microprobe analyses of hydrothermal potassic dioctahedral phyllosilicates.

Sample	AR9 90.6 m				AR9 166 m	AR9 264 m	AR82 552 m				AR82 655 m		AR18 39 m		AR18 266 m				AR18 249 m							
(wt%)																										
SiO ₂	46.40	48.52	48.67	47.27	53.04	50.60	53.04	46.41	46.35	47.31	48.40	46.93	44.39	48.50	47.99	46.73	48.20	47.72	48.01	45.74	45.73	50.93	46.76	46.95	47.77	47.36
TiO ₂	0.18	0.25	0.27	0.34	0.00	0.05	0.00	0.58	0.54	0.54	0.45	0.40	0.13	0.11	0.12	0.19	0.01	0.09	0.15	0.38	0.24	0.25	0.25	0.00	0.08	0.14
Al ₂ O ₃	35.67	37.77	38.09	36.17	36.89	35.62	36.89	35.31	36.38	34.63	33.07	35.60	36.24	34.23	34.14	33.14	34.69	35.64	34.76	33.79	34.12	34.08	33.51	35.98	34.91	36.24
⁵ FeO	0.83	0.21	0.36	1.67	1.04	0.88	1.04	0.33	0.10	0.28	0.34	0.11	0.54	0.95	0.96	1.38	1.75	0.48	0.90	1.61	2.24	0.92	0.89	0.74	0.95	0.43
MnO	0.01	0.00	0.02	0.07	0.00	0.02	0.00	0.05	0.00	0.02	0.00	0.00	0.00	0.00	0.00	0.01	0.00	0.03	0.00	0.00	0.00	0.00	0.01	0.01	0.02	0.03
MgO	1.46	1.30	1.29	1.49	1.27	0.91	1.27	1.24	0.74	1.30	1.85	1.88	0.16	0.90	0.75	1.02	0.89	0.81	1.06	0.36	0.46	1.70	1.09	0.48	1.64	0.45
CaO	0.03	0.00	0.00	0.04	0.15	0.18	0.15	0.00	0.00	0.00	0.05	0.03	0.01	0.03	0.01	0.06	0.06	0.00	0.02	0.01	0.02	0.00	0.00	0.00	0.02	0.02
SrO	0.08	0.06	0.08	0.07	0.05	0.06	0.05	0.06	0.05	0.09	0.06	0.05	0.12	0.08	0.12	0.10	0.11	0.08	0.06	0.08	0.09	0.00	0.03	0.10	0.10	0.04
BaO	0.00	0.16	0.15	0.00	0.09	0.08	0.09	0.19	0.24	0.15	0.06	0.17	0.00	0.06	0.03	0.11	0.02	0.00	0.10	0.00	0.05	0.00	0.05	0.16	0.26	0.12
Na ₂ O	0.23	0.25	0.22	0.32	0.11	0.06	0.11	0.13	0.12	0.10	0.10	0.11	0.22	0.20	0.24	0.25	0.22	0.18	0.17	0.30	0.37	0.00	0.35	0.34	0.20	0.19
K ₂ O	10.03	9.70	9.59	9.93	7.51	6.58	7.51	9.69	9.45	10.39	9.89	9.65	8.83	9.34	9.74	9.63	9.43	9.90	8.96	8.88	9.34	9.14	9.73	9.46	9.26	9.19
F	0.98	1.31	1.37	1.10	0.47	0.00	0.47	0.62	0.53	0.67	1.12	0.16	0.32	0.61	0.64	0.66	0.63	0.67	0.70	0.16	0.15	0.00	0.37	0.23	0.59	0.25
Cl	0.03	0.00	0.01	0.07	0.01	0.03	0.01	0.00	0.01	0.03	0.04	0.00	0.01	0.01	0.04	0.05	0.03	0.00	0.01	0.04	0.03	0.00	0.01	0.01	0.01	0.02
P ₂ O ₅	0.05	0.07	0.06	0.00	0.02	0.11	0.02	0.03	0.00	0.03	0.00	0.02	0.56	0.28	0.20	0.04	0.11	0.01	0.05	0.08	0.05	0.00	0.03	0.09	0.03	0.30
Total	95.56	99.05	99.61	98.08	100.46	95.16	100.46	94.39	94.29	95.25	94.94	95.05	91.40	95.04	94.71	93.08	95.89	95.33	94.64	91.36	92.81	97.02	92.91	94.46	95.59	94.65
Structural formulae based on 22 Oxygen atoms																										
^{IV} Si	6.10	6.10	6.09	6.07	6.48	6.51	6.49	6.16	6.14	6.24	6.36	6.13	6.10	6.39	6.36	6.32	6.31	6.39	6.32	6.29	6.23	6.53	6.32	6.23	6.26	6.25
^{IV} Al	1.90	1.90	1.91	1.93	1.52	1.49	1.51	1.84	1.86	1.76	1.64	1.87	1.90	1.61	1.64	1.68	1.69	1.61	1.68	1.71	1.77	1.47	1.68	1.77	1.74	1.75
Octahedral																										
^{VI} Al	3.63	3.70	3.70	3.55	3.80	3.92	3.80	3.69	3.82	3.63	3.49	3.61	3.96	3.70	3.69	3.60	3.67	3.70	3.71	3.77	3.72	3.67	3.66	3.86	3.65	3.89
Ti	0.02	0.02	0.02	0.03	0.00	0.00	0.00	0.06	0.05	0.05	0.04	0.04	0.01	0.01	0.01	0.02	0.00	0.01	0.01	0.04	0.02	0.02	0.03	0.00	0.01	0.01
Fe	0.09	0.02	0.04	0.18	0.11	0.09	0.11	0.04	0.01	0.03	0.04	0.01	0.06	0.10	0.11	0.16	0.19	0.05	0.10	0.19	0.25	0.10	0.10	0.08	0.10	0.05
Mn	0.00	0.00	0.00	0.01	0.00	0.00	0.00	0.01	0.00	0.00	0.00	0.00	0.00	0.00	0.00	0.00	0.00	0.00	0.00	0.00	0.00	0.00	0.00	0.00	0.00	0.00
Mg	0.29	0.24	0.24	0.29	0.23	0.17	0.23	0.25	0.15	0.26	0.36	0.36	0.03	0.18	0.15	0.21	0.17	0.16	0.21	0.07	0.09	0.32	0.22	0.10	0.32	0.09
ΣVI	4.03	3.99	4.01	4.06	4.14	4.19	4.14	4.03	4.03	3.97	3.94	4.02	4.07	3.99	3.96	3.99	4.04	3.93	4.03	4.06	4.09	4.12	4.01	4.04	4.09	4.05
Ca	0.00	0.00	0.00	0.01	0.02	0.02	0.02	0.00	0.00	0.00	0.01	0.00	0.00	0.00	0.00	0.01	0.01	0.00	0.00	0.00	0.00	0.00	0.00	0.00	0.00	0.00
Na	0.06	0.06	0.05	0.08	0.03	0.01	0.02	0.03	0.03	0.03	0.03	0.04	0.06	0.05	0.06	0.06	0.06	0.05	0.05	0.08	0.10	0.00	0.09	0.09	0.05	0.05
K	1.68	1.56	1.53	1.63	1.17	1.08	1.17	1.64	1.60	1.73	1.66	1.61	1.55	1.57	1.65	1.66	1.58	1.69	1.50	1.56	1.62	1.49	1.68	1.60	1.55	1.55
Ba	0.00	0.01	0.01	0.00	0.00	0.00	0.00	0.01	0.01	0.01	0.00	0.01	0.00	0.00	0.00	0.01	0.00	0.00	0.01	0.00	0.00	0.00	0.00	0.01	0.01	0.01
Sr	0.01	0.00	0.01	0.01	0.00	0.00	0.00	0.00	0.00	0.00	0.01	0.00	0.00	0.01	0.01	0.01	0.01	0.01	0.01	0.01	0.01	0.00	0.00	0.01	0.01	0.00
ΣInterlayer	1.74	1.62	1.59	1.71	1.22	1.13	1.22	1.69	1.64	1.77	1.69	1.66	1.61	1.63	1.71	1.74	1.64	1.74	1.56	1.64	1.73	1.50	1.77	1.70	1.62	1.61
F	0.41	0.52	0.54	0.45	0.18	0.00	0.18	0.26	0.22	0.28	0.47	0.46	0.14	0.25	0.27	0.28	0.27	0.28	0.29	0.07	0.07	0.00	0.16	0.10	0.24	0.10
Cl	0.01	0.00	0.00	0.02	0.00	0.01	0.00	0.00	0.00	0.01	0.01	0.00	0.00	0.00	0.01	0.01	0.01	0.00	0.00	0.01	0.01	0.00	0.00	0.00	0.00	0.00

1. All iron as Fe²⁺.
ΣVI: sum. of octahedral cations.

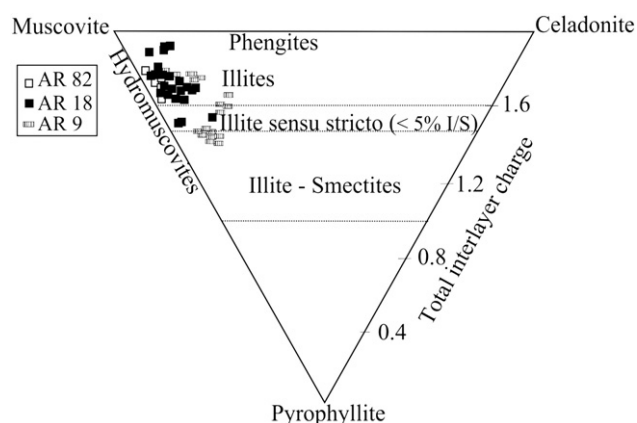


Fig. 7. Compositions of potassic dioctahedral phyllosilicates in the muscovite–celadonite–pyrophyllite triangular coordinates (Newman and Brown, 1987).

telescoping of these two mineral assemblage is interpreted as a consequence of the progressive degradation of the paleosurface (exhumation) due to regional uplift (and concomitant rapid erosion) of Sierras Pampeanas along NE-striking faults (Allmendinger, 1986; Bissig et al., 2001; Jordan and Allmendinger, 1986; Sasso, 1997; Sasso and Clark, 1998). In the E–W 6969400 N section of the Agua Rica deposit examined, the polymetallic epithermal alteration–mineralization stages are superimposed upon older porphyry Cu–Mo mineral assemblages.

Biotite from early potassic alteration patches are preserved in the Seca Norte porphyry, which contains moderate hypogene Cu and Au

grades (Fig. 2C). Based on preliminary microthermometric data on early quartz veinlets (Franchini et al., 2011), porphyry-style potassic alteration and mineralization was produced between 375 and >500 °C, by hypersaline fluids (and vapor) with intermediate S fugacity according to the dominant sulfides mineralogy (mainly pyrite + chalcopyrite molybdenite ± bornite) and gold deposited at intermediate sulfidation states (Einaudi et al., 2003).

Fig. 8A and B show the recalculated fugacity ratios of hydrothermal fluids determined from biotite associated with potassic alteration for Agua Rica using the equations of Munoz (1992) and the upper and lower temperatures estimated for the potassic alteration from fluid inclusion in early quartz veinlets (Franchini et al., 2011). Based on these calculations, high temperature (550 °C) hydrothermal fluids associated with the potassic alteration possessed $\log f_{\text{H}_2\text{O}}/\text{HF}$ and $\log f_{\text{H}_2\text{O}}/\text{HCl}$ values lower than cooler hydrothermal fluids (370 °C). In contrast, the $\log (f_{\text{HF}}/f_{\text{HCl}})$ is higher in the high temperature population. The recalculated fugacity ratios determined from biotite associated with potassic alteration for eight porphyry Cu deposits (see Selby and Nesbitt, 2000 and references therein) have been added for comparison (Fig. 8A and B). Hydrothermal fluids associated with potassic alteration at Agua Rica possessed $\log f_{\text{H}_2\text{O}}/\text{HF}$ values lower than those determined for the other porphyry Cu deposits, but higher than those for porphyry Mo mineralization (4.3–4.6 for Henderson, Selby and Nesbitt, 2000 and references therein). As suggested previously by Brimhall and Crerar (1987) these differences may be a function of the magma source and the geochemical processes associated with the evolution of the melt. The composition of the Agua Rica magmas fall between the A-type magmas of the Climax-type porphyry molybdenite deposits (like Henderson) formed in areas of crustal relaxation and extension (Ludington and Plumlee,

Table 3
Representative microprobe analyses of hydrothermal pyrophyllite.

Sample	AR82–96.1 m			AR82–146.8			AR82–248 m			AR82–279 m			AR82–333 m			AR18–85 m			AR18–141.2 m			AR18–266 m			AR80–86.7 m		
SiO ₂	61.37	62.94	64.21	66.08	64.89	55.70	62.79	58.60	63.01	66.62	57.14	63.37	64.75	64.75	54.75	55.37	63.45	68.14									
TiO ₂	0.00	0.02	0.03	0.00	0.03	0.00	0.00	0.00	0.02	0.00	0.09	0.00	0.03	0.03	0.00	0.00	0.00	0.18									
Al ₂ O ₃	29.53	30.78	29.71	30.43	30.09	27.56	30.74	29.38	30.20	29.62	26.52	28.99	29.38	29.38	27.99	26.46	27.43	29.09									
¹ FeO	0.05	0.06	0.37	0.06	0.33	0.28	0.23	0.19	0.13	0.10	0.07	0.12	1.17	1.17	0.54	0.20	0.12	0.09									
MnO	0.00	0.00	0.00	0.02	0.00	0.03	0.00	0.03	0.00	0.03	0.00	0.01	0.01	0.01	0.01	0.02	0.04	0.00									
MgO	0.00	0.01	0.00	0.02	0.04	0.01	0.01	0.00	0.01	0.00	0.01	0.02	0.01	0.01	0.00	0.00	0.00	0.02									
CaO	0.06	0.06	0.04	0.07	0.08	0.27	0.04	0.05	0.06	0.02	0.09	0.06	0.03	0.03	0.16	0.08	0.01	0.05									
SrO	0.08	0.11	0.08	0.12	0.11	0.09	0.04	0.09	0.05	0.09	0.07	0.03	0.06	0.06	0.10	0.11	0.12	0.08									
BaO	0.00	0.02	0.00	0.00	0.10	0.02	0.09	0.00	0.00	0.00	0.07	0.04	0.03	0.03	0.06	0.12	0.01	0.07									
Na ₂ O	0.00	0.10	0.11	0.10	0.21	0.09	0.28	0.07	0.15	0.16	0.29	0.29	0.18	0.18	0.39	0.23	0.07	0.08									
K ₂ O	0.10	0.13	0.05	0.04	0.27	0.29	0.27	0.03	0.05	0.03	0.22	0.20	0.14	0.14	0.53	0.22	0.03	0.05									
F	0.34	0.28	0.27	0.21	0.30	0.28	0.17	0.23	0.26	0.29	0.35	0.30	0.09	0.09	0.10	0.14	0.32	0.22									
Cl	0.01	0.03	0.04	0.00	0.08	0.02	0.17	0.01	0.04	0.00	0.06	0.10	0.04	0.04	0.11	0.09	0.02	0.01									
P ₂ O ₅	0.02	0.02	0.04	0.02	0.03	0.01	0.02	0.00	0.00	0.03	0.00	0.00	0.00	0.00	0.03	0.00	0.00	0.04									
Total	91.44	94.45	94.82	97.09	96.41	84.52	94.76	88.58	93.86	96.87	84.82	93.38	95.87	95.87	84.70	82.97	91.47	98.03									
Structural formulae based on 22 Oxygen																											
Tetrahedral																											
^{IV} Si	7.69	7.65	7.78	7.79	7.74	7.59	7.63	7.60	7.69	7.86	7.73	7.78	7.78	7.79	7.50	7.68	7.92	7.95									
^{IV} Al	0.31	0.35	0.22	0.21	0.26	0.41	0.37	0.40	0.31	0.14	0.27	0.22	0.22	0.21	0.50	0.32	0.08	0.05									
Octahedral																											
^{VI} Al	4.04	4.06	4.02	4.01	3.97	4.02	4.03	4.07	4.03	3.98	3.96	3.97	3.95	3.99	4.02	4.01	3.96	3.94									
Ti	0.00	0.00	0.00	0.00	0.00	0.00	0.00	0.00	0.00	0.00	0.01	0.00	0.00	0.00	0.00	0.00	0.00	0.02									
Fe	0.01	0.01	0.04	0.01	0.03	0.03	0.02	0.02	0.01	0.01	0.01	0.01	0.12	0.01	0.06	0.02	0.01	0.01									
Mn	0.00	0.00	0.00	0.00	0.00	0.00	0.00	0.00	0.00	0.00	0.00	0.00	0.00	0.00	0.00	0.00	0.00	0.00									
Mg	0.00	0.00	0.00	0.00	0.01	0.01	0.01	0.01	0.01	0.00	0.00	0.00	0.00	0.00	0.00	0.00	0.00	0.00									
SVI	4.05	4.06	4.06	4.02	4.01	4.06	4.06	4.10	4.05	3.99	3.98	3.99	4.07	4.01	4.08	4.03	3.97	3.97									
Ca	0.01	0.01	0.01	0.01	0.01	0.04	0.01	0.01	0.01	0.00	0.01	0.01	0.00	0.01	0.02	0.01	0.00	0.01									
Na	0.00	0.00	0.03	0.02	0.05	0.02	0.07	0.01	0.04	0.04	0.08	0.07	0.04	0.05	0.10	0.06	0.02	0.02									
K	0.02	0.02	0.01	0.02	0.04	0.05	0.04	0.01	0.01	0.00	0.04	0.03	0.02	0.01	0.09	0.04	0.00	0.01									
Ba	0.00	0.00	0.00	0.00	0.00	0.00	0.00	0.00	0.00	0.00	0.00	0.00	0.00	0.00	0.00	0.01	0.00	0.00									
Sr	0.01	0.01	0.01	0.01	0.01	0.04	0.00	0.01	0.00	0.01	0.01	0.00	0.00	0.01	0.01	0.01	0.01	0.01									
ΣInterlayer	0.03	0.03	0.04	0.05	0.10	0.16	0.12	0.02	0.05	0.04	0.13	0.11	0.07	0.08	0.22	0.12	0.02	0.03									
F	0.13	0.11	0.02	0.08	0.11	0.12	0.07	0.09	0.10	0.11	0.15	0.12	0.03	0.09	0.04	0.06	0.13	0.08									
Cl	0.00	0.01	0.01	0.01	0.02	0.00	0.03	0.00	0.01	0.00	0.01	0.02	0.01	0.00	0.03	0.02	0.00	0.00									

1. All iron as Fe²⁺.

SVI: sum. of octahedral cations.

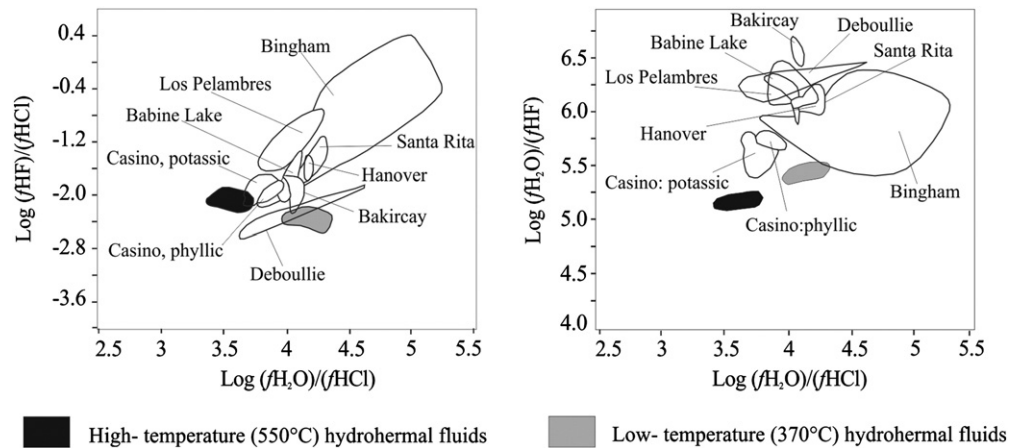


Fig. 8. Log (HF)/(HCl) versus log H_2O/HCl and B) Log H_2O/HF versus log H_2O/HCl of hydrothermal fluids from the potassic alteration of the Agua Rica deposit based on the equations of Munoz (1992) and the upper and lower temperatures estimated from fluid inclusions (Franchini et al., 2011).

2009) and the porphyry Cu–Mo deposits related to intermediate to felsic calc-alkaline magmas in volcano-plutonic arcs above active subduction zones (John et al., 2010).

Diocahedral phyllosilicates, mostly illite in composition, are the major component of the pervasive phyllic alteration (Fig. 3). They accompany the assemblage quartz + pyrite + covellite + molybdenite + rutile and B-type veinlets with molybdenite. Based on metal grades (Fig. 2C) this stage which was Mo-rich (Trampeadero porphyry, Franchini et al., 2011), did not add Cu, Au, and As in the altered zone, and some of the stockwork quartz veinlets have apparently been striped/leached of their former sulfides during the phyllic overprinting process (see Franchini et al., 2011). The mineralogy and textures of minerals encountered in the phyllic halo suggest the influence of at least two successive phenomenon: (1) cooling of hydrothermal fluids that expanded outward and upwards from the potassic alteration zones in both porphyries may have caused the biotite breakdown to mica-like diocahedral phyllosilicate and rutile, as well as K-feldspar replacement, and (2) due to telescoping of the system, the low to intermediate sulfidation chalcopryrite and bornite assemblage have been reconstituted as high sulfidation covellite and any early iron oxide may have been transformed into pyrite. Hydrothermal fluids may have achieved a very high sulfidation state at temperatures near 350 °C (Einaudi et al., 2003) and the resulting high H_2S/Fe ratio prevented deposition of Au (William-Jones and Heinrich, 2005). Illite may have been formed as the temperature of the hydrothermal fluids declined below 300 °C (Seedorff et al., 2005). When projected in the K + Na versus tetrahedral Si diagram (Fig. 9) the punctual analyses of potassic diocahedral phyllosilicates of the phyllic alteration from Agua Rica fall in the same compositional field than those from other porphyry copper deposits

worldwide which display a continuous trend between muscovite and illite composition (Parry et al., 2002 and references there in).

Locally illite and minor amounts of smectite are preserved in the clasts of the hydrothermal breccias from the epithermal stage containing some relics of phyllic alteration (Fig. 3). Illite and smectite may also represent two distinct thermal events, the cooler of which being marked by smectite. The anomalous Al contents in illites reflected in the diagrams of Figs. 5 and 7, cannot be related to an increase of pyrophyllite substitution or mixture with discrete pyrophyllite. It could be related to the presence of submicroscopic inclusions of later Al-rich minerals (kaolinite, zunyite, diasporite) superimposed over the illitic matrix of the phyllic halo.

The occurrence of pyrophyllite above an andalusite zone identified at depth is considered as a part of the pre-brecciation advanced argillic alteration stage formed from very acidic fluids probably originated during the absorption of early spent porphyry ore fluids, which had expanded to a low-density vapor, by heated ground water (William-Jones and Heinrich, 2005). Pyrophyllite replaces white micas, suggesting temperatures of formation between 280 and 360 °C (cf. Hemley et al., 1980). This stage has not contributed Cu and Au to the total metal content of the Agua Rica system.

A new emplacement of magma at shallow depth and fluids exsolution, expansion, and unroofing associated with release of mechanical energy, produced hydrothermal brecciation (formation of interfingering granite and hydrothermal heterolithic and monolithic breccias) and subsequent multistage advanced argillic alteration and mineralization at temperatures near 300 °C (svanbergite ± woodhouseite ± diasporite ± zunyite and Fe–Cu–As–Sn–S, Fe–Au–Ag–Bi–S, and Zn–Pb–S mineralization stages; Franchini et al., 2011). Later advanced argillic alteration stages precipitated locally dickite (<270 °C; Reyes, 1990) in the advanced argillic alteration envelope, and widespread kaolinite downwards, in the phyllic halo with superposed alunite–pyrite veinlets, as late mineral in clots or in veinlets thus, in these zones, fluid cooled enough for its formation (<200 °C; Reyes, 1990).

5.2. Metallurgical considerations

Besides of their interest in better understanding the time-space evolution of the hydrothermal activity of porphyry copper deposits, the spatial distribution of secondary phyllosilicates (Fig. 3) could be also of primary importance for the ore processing. Agua Rica is a world-class Cu–Au–Mo deposit which will be mined soon. The Agua Rica ores are proposed to be processed locally via differential flotation to produce separate copper and molybdenum concentrates. The traditional mineral processing plant operations will consist of crushing,

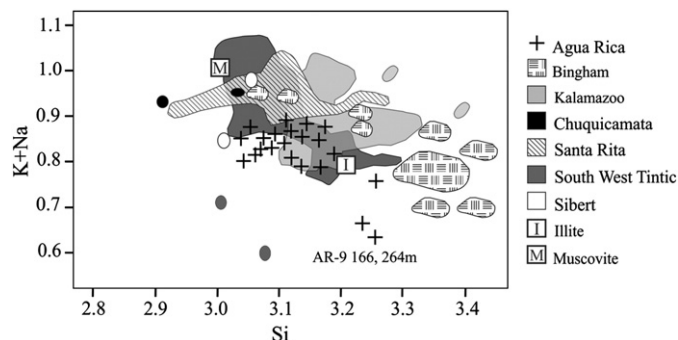


Fig. 9. Agua Rica illite compositions compared to illite from other porphyry copper deposits. Compositions of micas are from Bingham, Chuquicamata, and Kalamazoo (Guilbert and Schafer, 1979), Sibert (Beaufort and Meunier, 1983), Santa Rita and southwest Tintic (Parry et al., 1984), and Bingham (Parry et al., 2002).

grinding, separation and concentration of copper and molybdenum concentrates by flotation, tailings disposal.

Little work has been done to determine the influence of aluminosilicate minerals on the flotation of porphyry copper ores (Bulatovic et al., 1999). The presence of aluminosilicate minerals in copper flotation causes different problems, such as (a) loss in recovery, (b) increases of reagent consumption by fine particles; (c) the transfer of large quantities of clay minerals into the concentrate (d) increase in the quantities of fine particles in the crushing and grinding circuits; and (e) the flocculation phenomenon in the froth zone (Bulatovic, 2007; Bulatovic et al., 1999). Because of its hydrophobic behavior, pyrophyllite can pose challenges in the selective flotation of molybdenite. A predominant feature of molybdenite is that it is one of very few naturally occurring hydrophobic minerals. Several studies have been carried out to assess and differentiate the actual mechanism behind this rare phenomenon (Chander and Fuerstenau, 1972; Woods, 1976). As well, the effective use and application of selected promoters, frothers, regulators, activators, dispersants and depressants as flotation reagents in molybdenite flotation has been studied and reviewed in detail (Crozier, 1979, 1980; Rao, 1974).

To best evaluate and quantify the propensity of phyllosilicates to impede copper and molybdenum concentrate separation, recovery and grades, it will be imperative to accumulate representative bulk samples of the Agua Rica deposit. This includes samples from areas of differing mineralogy (Fig. 3) and grades (Fig. 2) to gauge the impact of these types of ores on any proposed plant. Then carefully planned and controlled comprehensive liberation and flotation testing should be undertaken in conjunction with mineralogical analysis to optimize and quantify recoveries, separations, grades and gangue deportment.

6. Concluding remarks

Our investigations on the spatial distribution and composition of phyllosilicate minerals in the porphyry copper-epithermal system of the Agua Rica world-class Cu–Au–Mo deposit outline several distinctive mineralogical zones (i.e. biotite, illite, pyrophyllite, and kaolinite-dickite zones) which differ not only by their hydrothermal history but also by their potential behavior during the ore processing operations.

Should processing of the phyllosilicates prove problematic, further systematic optimized testing of proven industrial gangue dispersants such as sodium silicate and soda ash should be undertaken. These have proven effective on limiting clays, talc and micas from molybdenum flotation concentration. As well, recent advances in hydrometallurgical processing (Anderson et al., 2011) may allow bulk combined copper and molybdenum concentrates to be treated. This would alleviate many complications in differential flotation separation, grade and recovery challenges posed by hydrophobic phyllosilicates as the emphasis would then be on recovery and not on separation or grade criteria. This may provide a more tenable path forward for development of the Agua Rica deposit should traditional mineral processing prove prohibitive.

Acknowledgments

This work forms part of a project financed by Consejo Nacional de Investigaciones Científicas y Técnicas Argentino (CONICET; PIP no 6043 and 1083), and Facultad de Ingeniería, U.N. del Comahue (PIP no. 04/1002). We would like to thank Dr. Pablo Marcet and Dr. J. L. Martín, managers of the Agua Rica Mining Company, for allowing us to collect samples for this study and consult unpublished reports from the Agua Rica project and to Dave Lentz (New Brunswick University) for collaboration with microprobe data. We are especially grateful to Lic. Claudio Devaux, Lic. Pedro Ruiz and their assistants in Andalgalá, and to Lic. López and Lic. Gobbo for their help in the field.

References

- Allmendinger, R.W., 1986. Tectonic development, southeastern border of the Puna Plateau. *Geological Society of America Bulletin* 97, 1070–1082.
- Anderson, C.G., Fayram, T.S., Twidwell, L.G., 2011. An update on industrial NSC pressure oxidation of combined copper and molybdenum concentrates. In: Casas, J.M., Lightfoot, C., Tapia, G. (Eds.), *Proceedings of the 6th International Seminar on Copper Hydrometallurgy*, Gecamin, Santiago, Chile, pp. 47–60.
- Beaufort, D., Meunier, A., 1983. A petrographic study of phyllic alteration superimposed on potassic alteration: the Sibert porphyry copper deposit (Rhône, France). *Economic Geology* 78, 1514–1527.
- BHP, 1999. The Agua Rica porphyry Cu–Mo–Au deposit, Catamarca. *Geology and Mineral Resource Update*, Internal report. 420 pp.
- Bissig, T., Lee, J.K.W., Clark, A.H., Heather, K.B., 2001. The Cenozoic history of volcanism and hydrothermal alteration in the central Andean flat-slab region: new ⁴⁰Ar–³⁹Ar constraints from the El Indio-Pascua Au (Ag, Cu) belt, 29° 20′–30° 30′ S. *International Geology Review* 43, 312–340.
- Brimhall, G.H., Crerar, D.A., 1987. Ore Fluids: Magmatic to Supergene. In: Carmichael, I.S.E., Eugster, H.P. (Eds.), *Thermodynamic modeling of geological materials: minerals, fluids and melts*. Mineralogical Society of America Reviews in Mineralogy 17, 10, 235–321.
- Brindley, G.W., Kao, C.C., Harrison, J.L., Lipsicas, M., Raythatha, R., 1986. Relation between structural disorder and other characteristics of kaolinites and dickites. *Clays and Clay Minerals* 34, 239–249.
- Bulatovic, S.M., 2007. *Handbook of Flotation Reagents, Chemistry, Theory and Practice. Flotation of Sulfide Ores*, Vol. 1. Elsevier, Amsterdam.
- Bulatovic, S., Wyslouzil, D.M., Kant, C., 1999. Effect of clay slimes on copper, molybdenum flotation from porphyry ores. In: Hancock, B.A., Pen, M.R.L. (Eds.), *Proceedings of Copper 99–Cobre 99 International Environment Conference*, Mineral Processing/Environment, Health and Safety, vol. II. The minerals, Metals and Materials Society.
- Caelles, J.C., Clark, A.H., Farrar, E., McBride, S.L., 1971. Quirt S. Potassium-argon ages of porphyry copper deposits and associated rocks in the Farallón Negro-Capillitas district, Catamarca, Argentina. *Economic Geology* 66, 961–964.
- Chander, S., Fuerstenau, D.W., 1972. On the natural floatability of molybdenite. *Transactions of the Society of Mining Engineers of AIME* 252, 62.
- Christidis, G.E., Eberl, D.D., 2003. Determination of layer-charge characteristics of smectites. *Clays and Clay Minerals* 51, 644–655.
- Crozier, R., 1979. Flotation reagents. In: Sutulov, A. (Ed.), *International Molybdenum Encyclopedia, 1778–1978. Processing and Metallurgy*, Vol. 2. Intermet Publications, Santiago, Chile.
- Crozier, R.D., 1980. Frother function in Sulphide flotation. *Mining Magazine* 26.
- Deer, W.A., Howie, R.A., Zussman, J., 1992. *An Introduction to the Rock Forming Minerals*, second ed. Prentice Hall, New York. 712 pp.
- Einaudi, M.T., Hedenquist, J.W., Inan, E., 2003. Sulfidation state of hydrothermal fluids: the porphyry-epithermal transition and beyond. In: Simmons, S.F., Graham, I.J. (Eds.), *Volcanic, geothermal and ore-forming fluids: Rulers and witnesses of processes within the Earth*. Society of Economic Geologists and Geochemical Society, Special Publication, 10, pp. 285–313.
- Franchini, M.B., Impicini, A., Lentz, D., Ríos, F.J., O'Leary, S., Pons, J., Schalamuk, I.A., 2011. Porphyry to epithermal transition in the Agua Rica polymetallic deposit, Catamarca, Argentina: an integrated petrologic analysis of ore and alteration parageneses. *Ore Geology Review* 41, 49–74.
- Guilbert, J.M., Schafer, R.W., 1979. Preliminary geochemical characterization of muscovites in porphyry base-metal alteration assemblages. *Nevada Bureau of Mines and Geology Report* 33, 57–68.
- Gustafson, L.B., Hunt, J.P., 1975. The porphyry copper deposit at El Salvador, Chile. *Economic Geology* 70, 857–912.
- Hemley, J.J., Montoya, J.W., Marinenko, J.W., Luce, R.W., 1980. Equilibria in the system Al₂O₃–SiO₂–H₂O and some general implications for alteration-mineralization processes. *Economic Geology* 75, 210–228.
- John, D.A., Ayuso, R.A., Barton, M., Blakely, R., Bodnar, R., Dilles, J., Gray, F., Graybeal, F., Mars, J., McPhee, D., Seal, R., Taylor, R., Vikre, P., 2010. *Porphyry Copper Deposit Model. Scientific Investigations*. U.S. Department of the Interior. U.S. Geological Survey, Reston, Virginia Report 2010–5070. 169 pp.
- Jordan, T.E., Allmendinger, R.W., 1986. The Sierra Pampeanas of Argentina: a modern analog of Rocky Mountain foreland deformation. *American Journal of Science* 286, 737–764.
- Koukharsky, M., Mirré, J.C., 1976. Mi Vida prospect: a porphyry copper-type deposit in northwestern Argentina. *Economic Geology* 71, 849–863.
- Landtwing, M., Dillenbeck, E., Leake, M., Heinrich, C., 2002. Evolution of the breccia-hosted porphyry-Cu–Mo–Au deposit at Agua Rica, Argentina: progressive unroofing of a magmatic-hydrothermal system. *Economic Geology* 97, 1273–1292.
- Ludington, S., Plumlee, G.S., 2009. Climax-type porphyry molybdenum deposits U.S. Department of the Interior U.S. Geological Survey. Open-File Report 2009–1215. 16 pp.
- Moore, D.M., Reynolds, R.J.R., 1997. *X-Ray Diffraction and the Identification and Analysis of Clay Minerals*. Oxford University Press, New York. 378 pp.
- Munoz, J.L., 1984. F–OH and Cl–OH exchange in micas with applications to hydrothermal ore deposits. In: Bailey, S.W. (Ed.), *Micas*. Reviews in Mineralogy 13, 469–494.
- Munoz, J.L., 1992. Calculation of HF and HCl fugacities from biotite compositions: revised equations. *Geological Society of America, Abstracts with Programs* 24, A221.
- Navarro, H., 1986. Geología general y económica del pórfido de cobre-molibdeno “Mi Vida”, Andalgalá, Catamarca. *Revista del Instituto de Geología, Universidad Nacional de Jujuy* 6, 127–154.
- Newman, A., Brown, G., 1987. The chemical constitution of clays. In: Newman, A. (Ed.), *Chemistry of Clays and Clay Minerals*. Mineralogical Society Monograph No 6. 129 pp.

- Parry, W.T., Ballantyne, J.M., Jacobs, D.C., 1984. Geochemistry of hydrothermal sericite from Roosevelt Hot Springs, and the Tintic and Santa Rita porphyry copper systems. *Economic Geology* 79, 72–86.
- Parry, W.T., Jasumback, M., Wilson, P.N., 2002. Clay mineralogy of phyllic and intermediate argillic alteration at Bingham, Utah. *Economic Geology* 97, 221–239.
- Perelló, J., Rojas, N., Devaux, C., Fava, L., Etchart, E., Harman, P., 1998. Discovery of the Agua Rica porphyry Cu–Mo–Au deposit, Catamarca Province, northwestern Argentina, Part II: Geology. In: Porter, T.M. (Ed.), *Porphyry and hydrothermal copper and gold deposits, a global perspective: Glenside, South Australia: Australian Mineral Foundation, Symposium, Perth, Western Australia*, pp. 117–132.
- Rao, S.R., 1974. Surface forces in flotation. *Minerals Science and Engineering* 16 (1), 45.
- Reyes, A.G., 1990. Petrology of Philippines geothermal systems and the application of alteration mineralogy to their assessment. *Journal of Volcanology and Geothermal Research* 43, 279–309.
- Reynolds Jr., R.C., Reynolds III, R.C., 1996. NEWMOD®, NEWMOD for Windows™, the Calculation of One-Dimensional Diffraction Patterns of Mixed-Layered Clay Minerals: Hanover, New Hampshire.
- Sasso, A.M., 1997. Geological evolution and metallogenetic relationships of the Farallón Negro volcanic complex, NW Argentina. PhD thesis, Queen's University, Kingston, Ontario. 843 pp.
- Sasso, A.M., Clark, A.H., 1998. Magmatic, hydrothermal and tectonic evolution and implications for Cu–Au metallogeny in the Andean back-arc. *Society of Economic Geologists (SEG) Newsletter* 34 (1), 8–17.
- Seedorff, E., Dilles, J.H., Proffett Jr., J.M., Einaudi, M.T., Zurcher, L., Stavast, W.J.A., Johnson, D.A., Barton, M.D., 2005. Porphyry deposits—characteristics and origin of hypogene features: Society of Economic Geologists: *Economic Geology* 100th Anniversary, Vol. 1905–2005, pp. 251–298.
- Selby, D., Nesbitt, B.E., 2000. Chemical composition of biotite from the Casino porphyry Cu–Au–Mo mineralization, Yukon, Canada: evaluation of magmatic and hydrothermal fluid chemistry. *Chemical Geology* 171, 77–93.
- Velde, B., 1985. *Clay minerals: a physico-chemical explanation of their occurrence: developments in Sedimentology*. Elsevier, Amsterdam. 427 pp.
- William-Jones, A., Heinrich, C.A., 2005. Vapor transport and the formation of magmatic-hydrothermal ore deposits. *Economic Geology* 100, 1287–1312.
- Woods, R., 1976. Electrochemistry of sulphide flotation. In: Fuerstenau, M.C. (Ed.), *Flotation: A.M. Gaudin Memorial Volume, 1*. American Institute of Mining, Metallurgical and Petroleum Engineers, New York, p. 298.